J. R. Clark, M. A. Abdelmoneum, C. T.-C. Nguyen, "UHF high-order radial-contour mode disk resonators," *Proceedings,* 2003 IEEE Int. Frequency Control Symposium, Tampa, Florida, May 5-8, 2003, pp. 802-809.

UHF High-Order Radial-Contour-Mode Disk Resonators

John R. Clark, Mohamed A. Abdelmoneum, and Clark T.-C. Nguyen
Center for Wireless Integrated Microsystems, University of Michigan, Ann Arbor, MI

***Abstract*—A micromechanical, laterally vibrating disk resonator, fabricated via a technology combining polysilicon surface-micromachining and metal electroplating to attain sub-micron lateral capacitive gaps, has been demonstrated at frequencies as high as 829 MHz and with *Q*'s as high as 23,000 at 193 MHz. Furthermore, the resonators have been demonstrated operating in the first three radial contour modes, allowing a significant frequency increase without scaling the device, and a 193 MHz resonator has been shown operating at *atmospheric* pressure with a *Q* of 8,880 — evidence that vacuum packaging is not necessary for many applications. The geometric dimensions necessary to reach a given frequency are larger for this contour-mode than for the flexural-modes used by previous resonators. This, coupled with its unprecedented *Q* value, makes this disk resonator a choice candidate for use in the IF and RF stages of future miniaturized transceivers.**

I. Introduction

With recent frequency increases into the mid-VHF range [1,2], vibrating micromechanical ("μmechanical") resonators with *Q*'s approaching 100,000 [3] have emerged as leading candidates for on-chip versions of the low-loss, small percent bandwidth IF filters and the high-*Q* reference oscillator tanks required in wireless communication handsets. Having achieved the VHF frequencies needed for IF applications, μmechanical resonators now look towards the UHF frequencies needed for RF applications. As detailed in [4], μmechanical resonators are projected to make their biggest impact in RF applications, as the defining elements in RF channel-select filter banks and ultra-low power, low-phase noise synthesizers, both made possible by *Q*'s >5,000 and targeted for use in alternative transceiver architectures that trade power for *Q*.

Much like the case for transistors, extending the frequency of μmechanical resonators generally entails scaling of resonator dimensions. As a result, previous VHF demonstrations have used submicron dimensions to achieve higher frequencies—an approach that also reduced *Q*-limiting anchor losses by maintaining small values of resonator stiffness [1]. Unfortunately, smaller size often coincides with smaller power handling [5] and an increased susceptibility to environmental effects [6], such as contamination or thermal fluctuations. Although recently demonstrated free-free beam μmechanical resonators have been able to achieve frequencies up to 92 MHz with *Q*'s around 8,000 while avoiding submicron dimensions [2], whether or not they can maintain their size and *Q* at UHF frequencies has yet to be seen.

This work presents an alternative, perhaps superior, design based on the radial contour mode, or areal dilation, of a μmechanical disk structure capable of attaining very high frequencies while retaining relatively large dimensions. Using this disk design, operating in the fundamental mode, a frequency of 433MHz has been attained with a *Q* exceeding 4,000 using a disk with a diameter of 12.6 μm—slightly

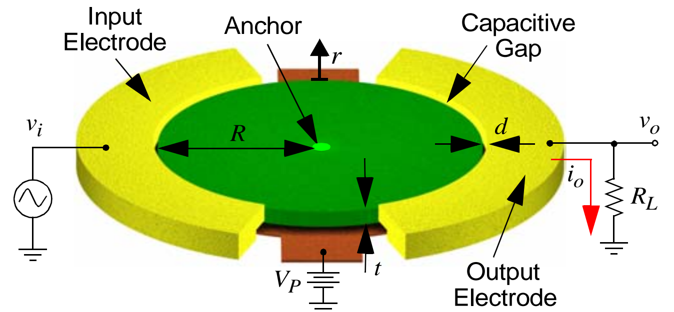

Fig. 1: Perspective view of a disk microresonator illustrating a preferred two-port bias and excitation scheme.

larger than the 11.3 μm required to attain only 92 MHz in previous free-free beam resonators. Disk resonators have also been tested operating in the second and third overtones, yielding frequencies as high as 829MHz. The resonators were evaluated using several different measurement techniques described herein, including an electromechanical mixing measurement technique intended to reduce parasitic effects at the resonant frequency, resulting in a vast improvement in the extracted *Q* value over a typical direct measurement, and in some cases enabling a measurement where direct techniques could not detect the resonant signal.

II. Device Description and Operation

Figure 1 presents a perspective-view schematic of the disk μresonator, identifying key dimensions and indicating a preferred (2-port) bias and excitation scheme. The resonator consists of a disk suspended 5,000 Å above the substrate with a single anchor at its center. Plated metal input electrodes surround the perimeter of the disk, separated by a narrow air (or vacuum) gap that defines the capacitive, electromechanical transducer of this device. As illustrated, the two electrodes surrounding the disk are positioned and spaced to allow routing to the structure while maintaining a symmetric distribution of electrostatic force. To operate the device, a DC bias voltage V_P is applied to the structure, while an AC input signal is applied to the input electrode, resulting in a time varying electrostatic force acting radially on the disk. When the input signal, and hence the force that it generates, are acting at the resonant frequency of the device, that force is effectively multiplied by the *Q* of the resonator, producing expansion and contraction of the disk along its radius, as shown in Fig. 2, which illustrates the shape of the fundamental mode. This motion, in turn, results in a time-varying, DC-biased capacitor between the disk and the output electrode generating an output current given by

$$i_o = V_P \frac{\partial C_o}{\partial r} \frac{\partial r}{\partial t} , \quad (1)$$

where r is the radial displacement at the edge of the disk and $\partial C_o / \partial r$ is the change in electrode-to-resonator sense capaci-

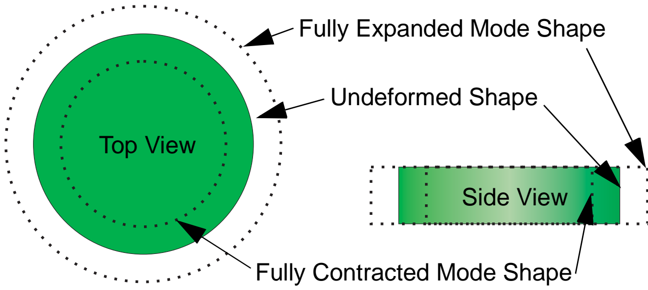

Fig. 2: Radial contour mode shape for the fundamental mode exhibits no rotational or flexural components

tance per unit displacement. The output current i_o can be sensed either directly as the voltage across the load resistor R_L, or via a transimpedance amplifier. Note that if the resonator Q is the primary parameter to be measured, the load resistance R_L should be kept small in order to minimize Q-loading.

As indicated in Fig. 2, the radial contour mode constrains vibration of the resonator entirely within the plane of the device with no out-of-plane motion. In addition, the particular modes of this work exhibit no rotational motion around the centroid, leaving only extensional movement of the resonator mass and yielding a very high stiffness and frequency associated with longitudinal vibrations. An infinite number of higher overtones also exist which adhere to these restrictions. Figure 3 illustrates the first three such modes, all of which are measured within this work. Arrows indicate direction of vibration throughout one half-cycle, and shaded contours indicate relative displacement. In the fundamental mode, the entire disk is moving in-phase along the radius, with maximum displacement at the edges and a stationary nodal point in the center. In addition to the central node, the second mode adds a nodal circumference at which the resonator is also stationary and the phase of vibration reverses. The third mode adds yet another nodal circumference, creating three distinct vibrating regions. Additional n^{th}-order overtones are possible, with each mode having a central node and n-1 nodal circumferences.

Previous work on free-free beam μmechanical resonators has shown that resonators with relatively large dimensions exhibit higher stiffnesses than their submicron counterparts and thus can achieve high Q only if sufficiently isolated from the substrate so as to eliminate energy losses to it. In the particular free-free beam design of [2], isolation from the substrate was achieved in part by attaching support beams only at flexural-mode nodal points. The disk design of this work very conveniently allows a similar isolation strategy. In particular, because the motion of the disk is symmetric and purely radial at the desired resonance, anchoring the resonator at its central node, as shown in Fig. 1, then minimizes energy losses to the substrate, allowing high-Q operation despite the high stiffness of the design.

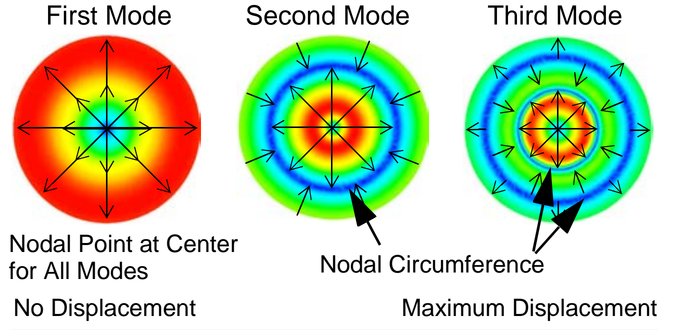

Fig. 3: Contour plots with colors indicating the relative magnitude of displacement and arrows indicating the relative direction for each mode shape.

III. Theory and Design

To facilitate the incorporation of disk resonators into filter and oscillator designs, equivalent models and analytical formulations for resonator properties (e.g., resonant frequency, impedance) are needed. These are addressed in the following subsections.

A. Geometric Frequency Design

The mechanical resonant frequency for the radial contour mode of a disk is governed mainly by its material properties and radius. Neglecting second order effects due to thickness and finite anchor dimensions, the resonant frequency may be determined by finding a numerical solution for f_o to the system of equations [7]

$$(\zeta/\xi)\frac{J_0(\zeta/\xi)}{J_1(\zeta/\xi)} = 1-\sigma , \quad (2)$$

$$\zeta = 2\pi f_o R\sqrt{\frac{\rho(2+2\sigma)}{E}} , \quad (3)$$

$$\xi = \sqrt{\frac{2}{1-\sigma}}, \quad (4)$$

where R is the radius of the disk; E, σ, and ρ are the Young's modulus, Poisson's ratio, and density, respectively, of its structural material; and $J_i(y)$ is the Bessel function of the first kind of order i. The solution to (2)-(4) is periodic, so that the frequency of the nth mode corresponds to the nth solution.

While representing a rigorous solution to the differential equations of vibration, this set of equations does not provide clear insight into how the individual parameters affect the frequency. By sacrificing some degree of accuracy, (2)-(4) can be rendered into the more intuitive form,

$$f_o = \frac{\kappa\alpha}{R}\sqrt{\frac{E}{\rho}}, \quad (5)$$

where κ is a parameter dependent upon Poisson's ratio (κ=0.342 for polysilicon [8]) and α depends on the order of the desired mode. Figure 4 shows the resonant frequency versus diameter for polysilicon disks, showing the inverse

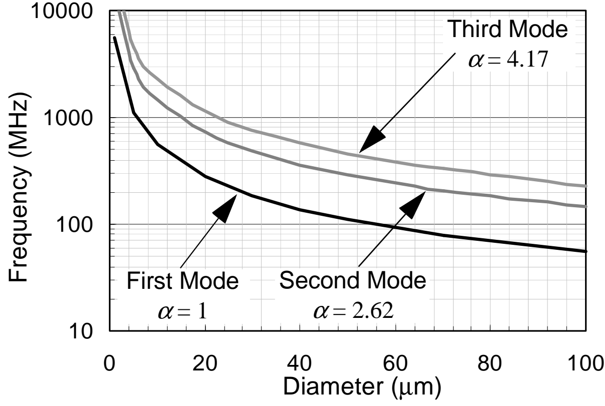

Fig. 4: Plot of frequency vs. diameter for a polysilicon disk.

relationship between frequency and size. In addition, Fig. 4 gives the values of α for the first three modes. The advantage of using higher overtones is clear; a 1GHz resonator operating in the first mode requires a diameter of 5.5 µm, while the second and third modes require 14.5 µm and 23.0 µm diameters respectively, helping to overcome potential lithography and power-handling issues as frequency scales. However, even in the fundamental mode, at the 900-1800 MHz RF frequencies commonly used in wireless handsets, the required diameters of 6.2 µm for 900 MHz and 3 µm for 1.8 GHz are well within the capabilities of present-day integrated circuit fabrication technology.

B. Equivalent Models

Once the resonant frequency has been determined, additional parameters such as equivalent circuit elements may be extracted to aid in system design. The lumped-element equivalent mechanical model is presented first and provides the underpinnings for the electrical model, which follows.

Equivalent Mechanical Model

As with any vibratory system, the disk resonator may be represented by a lumped-element equivalent mechanical model such as that depicted in Fig. 5. This model, composed of a rigid-body mass connected to a stationary base through spring and damper elements, aids in the design of more complex systems such as filters and serves as the basis for the electrical model described in the next section. The equivalent mass m_r at any given point on the perimeter of the disk is determined from the total kinetic energy in the resonator and the velocity at that point as given by [8]

$$m_r = \frac{KE_{tot}}{\frac{1}{2}V(R)^2} = \frac{2\rho\pi t}{V(R)^2}\int_0^R rV(r)^2\partial r = \frac{2\rho\pi t}{J_1(hR)^2}\int_0^R rJ_1(hr)^2\partial r \quad (6)$$

$$V(r) = \omega_o h J_1(hr) \quad (7)$$

$$h = \sqrt{\frac{\omega_o^2\rho}{\frac{2E}{2+2\sigma}+\frac{E\sigma}{1-\sigma^2}}}, \quad (8)$$

where KE_{tot} is the total peak kinetic energy in the vibrating system, $V(r)$ is the radial velocity of a point at a distance r from the center, t is the thickness of the disk, and $\omega_o=2\pi f_o$. Note that if R is determined from (2)-(4), then no changes in (6)-(9) are necessary to account for higher order modes. In turn, the effective stiffness k_r of the resonator is given by

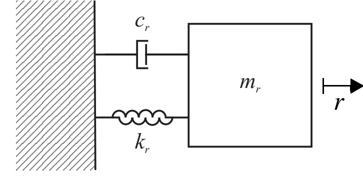

Fig. 5: Equivalent lumped-element mechanical model for a disk resonator consisting of a mass-spring-damper system.

$$k_r = \omega_o^2 m_r, \quad (9)$$

and finally, the value of the damping element is related to both m_r and k_r, as well as the Q of the resonator, by

$$c_r = \frac{\sqrt{k_r m_r}}{Q}. \quad (10)$$

In most cases, the Q of the resonator is difficult to predict theoretically, so the damping element is typically determined empirically. Also, note that the effective mass and stiffness on the perimeter of a radial contour mode disk are independent of location, indicating that all points on the circumference of the disk are moving with the same velocity, obviating the complex integration required to obtain accurate model parameters in flexural mode resonator counterparts [9].

The primary output variable of the mechanical model is the displacement of the mass, which is equivalent to the radial displacement of the perimeter of the disk. The amplitude of the displacement is given by

$$\Re = \frac{QC_oV_PV_i}{k_r d} \quad (11)$$

where V_i is the amplitude of the ac input signal, d is the electrode-to-resonator gap, and C_o is the static electrode-to-resonator capacitance of the input port.

Equivalent Circuit Model

The mechanical model introduced in the previous section may be transformed into an equivalent circuit of the form shown in Fig. 6, which presents an equivalent *RLC* circuit modeling the disk resonator of Fig. 1. In this circuit [9], the motional elements l_x, c_x, and $r_x$model the resonant behavior of the device and are directly related to the mass-spring-damper values, respectively, by

$$l_x = m_r, \quad (12)$$

$$c_x = \frac{1}{k_r}, \quad (13)$$

$$r_x = c_r. \quad (14)$$

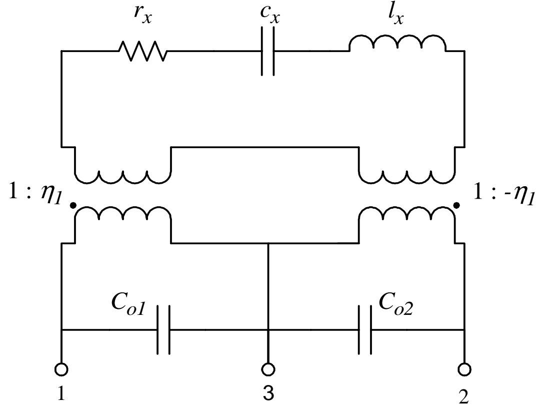

Fig. 6: Equivalent circuit model for a disk resonator with two ports. The model is comprised of an *RLC* tank to model the resonant behavior and transformers to model each port.

A transformer models the electromechanical transduction at each port, while the capacitor C_{on} models the capacitance between the nth port and the resonator body, consisting largely of the static capacitance between the electrode and disk but also including any additional parasitic capacitance between the ports. Comparing Fig. 6 with Fig. 1, Port 1 corresponds to the input electrode, Port 2 corresponds to the output electrode, and Port 3 corresponds to the port where the DC-bias is attached to the structure. The transformer at each port is characterized by the electromechanical coupling coefficient given by

$$\eta_n = V_P \frac{\partial C_{on}}{\partial r}. \tag{15}$$

The negative sign at the second port is included to ensure the proper current directions in the resonant tank loop — *i.e.* if the negative sign where omitted, an identical positive input voltage on Ports 1 and 2 would result in the currents canceling in the tank. If the number of ports on the device differs from the two shown in Fig. 6, then a transformer may be added (or removed) for each additional (or eliminated) port. Care should be taken when adding ports to the model to ensure that the transformer currents sum at the body port (Port 3 in the figure) and in the resonant tank loop to avoid the aforementioned current cancellation.

In many applications, the series motional resistance as seen from a single input port, designated R_x, must be minimized for impedance matching purposes. R_x is given by the impedance transformation of r_x,

$$R_x = \frac{r_x}{\eta_n^2} = \frac{c_r}{\eta_n^2} \tag{16}$$

According to the equations (10), (15), and (16), and assuming that Q is fixed, this is best accomplished by maximizing the dc-bias voltage V_P and the $\partial C_{on}/\partial r$ term. In many practical systems, however, the maximum voltage is often limited by either the transistor technology supporting the resonator or the available power supply, leaving $\partial C_{on}/\partial r$, which varies as (t/d^2), as the only adjustable parameter. Thickness t is limited by technology constraints and by second order effects that cause frequency to decrease as thickness increases, so $\partial C_{on}/\partial r$ is best increased by decreasing the electrode-to-resonator gap spacing d. Since $\partial C_{on}/\partial r$ varies as $(1/d^2)$, changes in d have a very strong effect on R_x, which is proportional to d^4. To illustrate the importance of d, a 200 MHz resonator with d=1 µm, t=2 µm, and V_P=20 V has an R_x=286 MΩ, which is excessively high, especially at RF frequencies. If the gap is reduced to 1000 Å while maintaining the other parameters, R_x decreases to 29 kΩ—strong justification for a disk resonator fabrication technology capable of realizing submicron lateral electrode-to-resonator gaps, such as that described in Section V.

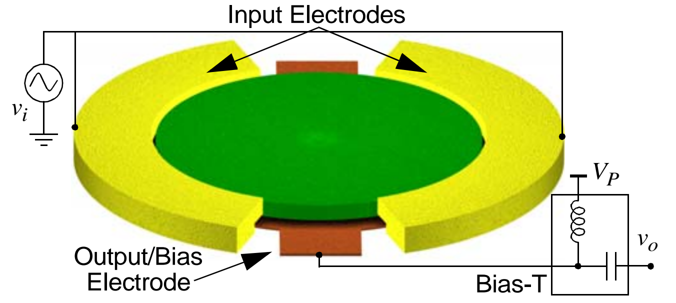

Fig. 7: Perspective view of a one-port measurement setup.

IV. Measurement Theory and Techniques

Several different approaches to measurement are possible with the disk structure [10]. The following sections present four such techniques and discuss their theory, advantages, and disadvantages. The work in [10] presents a more comprehensive comparison of measurement techniques beyond the scope of this work.

A. One-Port Measurement

The one-port, direct measurement scheme, depicted in Fig. 7 is the simplest to implement, as it requires only a single input electrode. The equivalent electrical circuit can be obtained by shorting Port 1 and Port 2 in Fig. 6. Referring to Fig. 6 and (16), at resonance, the impedance of the device is simply given by

$$Z_{in} = \frac{1}{\frac{1}{R_x} + j\omega_o C_o}. \tag{17}$$

Note that R_x has decreased by 4X over the two-port case because η has doubled, and that $C_o = C_{o1} + C_{o2}$. For sufficiently large values of C_o relative to R_x, the capacitance term dominates, resulting in a feed-through current that effectively masks the motional current derived from R_x. Furthermore, C_o creates a parallel-resonance whose frequency is given by

$$f_p = \frac{\sqrt{C_o + C_x}}{2\pi\sqrt{C_o C_x L_x}}, \tag{18}$$

where $C_x = \eta^2 c_x$ and $L_x = l_x/\eta^2$. C_o is typically much larger than C_x, so f_p is often very close to the series resonant frequency $f_o = 1/2\pi\sqrt{C_x L_x}$ and can distort the measured signal, shifting the resonant peak, altering the pass band, and making the true performance parameters of the resonator difficult to extract, especially the device Q.

To improve the ratio of C_o to R_x, the electromechanical coupling coefficient η should be increased. As discussed in the previous section, gap spacing is the most viable parameter to optimize. Hence, in subsequent device generations, the gap can be scaled in order to improve the ratio between R_x and the impedance of C_o, which is proportional to d^3. In order to ensure a measurable peak of at least 6 dB, this impedance ratio ($R_x/(1/\omega C_o)$) should be 0.5 or less.

B. Two-Port Measurement

If a second electrode is available, the two-port measurement scheme depicted in Fig. 1 can overcome the problems posed by C_o in a device with sub-optimal gap spacing. In this scheme, the dc bias is applied directly to the structure, while the input electrode is split in half. The ac input signal is applied to one of these electrodes, and the output motional current is detected from the other. With the electrode layout depicted, this excitation scheme results in a non-symmetric force used to excite a symmetric mode shape. However, so long as the force is applied at the frequency corresponding to the symmetric mode, the resultant vibration will assume the correct mode shape with only slight distortion.

Examining the schematic in Fig. 6, the body Port 3 is connected to an AC ground, and the static drive/sense capacitance has been split in half and shunted to ground. In addition, η is reduced by a factor of two over the one-port case because the electrode area has been halved, leading to a 4X reduction in output current magnitude. Despite the output signal reduction, this scheme enables a cleaner measure of resonator performance as the detrimental effects of C_o are negated by shunting the capacitance to ground.

C. Mixing Measurement

Even with separate input and output electrodes, feedthrough currents between the two electrodes may still exist (*e.g.* through the substrate) that can mask the motional current, so there is still a need to separate the motional current from extraneous parasitic currents. One approach is to use non-linear mixing to separate the currents in the frequency domain by exciting the resonator with a set of input frequencies different from the resonant frequency. The inherent nonlinearity of the parallel-plate capacitive transducer may be employed to mix these out-of-band electrical input signals to a force acting at the resonant frequency. This measurement technique may be implemented using an RF/LO (Local Oscillator) scheme as described in [11]. In this case, the two-port configuration is used, but v_i is replaced with

$$v_i = V_{RF}\cos\omega_{RF}t\,, \tag{19}$$

and an additional input signal v_{LO} is applied to the bias port through a bias-T such that

$$v_{LO} = V_{LO}\cos\omega_{LO}t \tag{20}$$

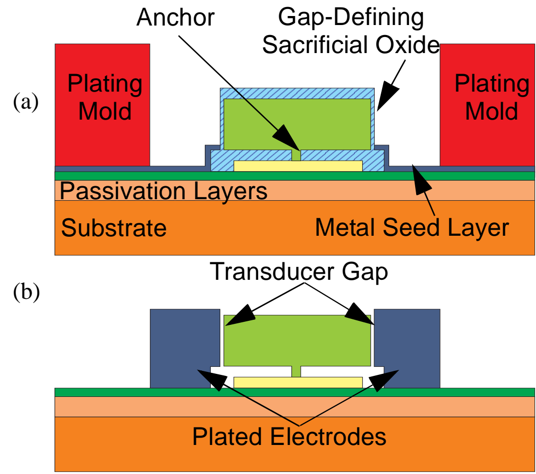

Fig. 8: Process cross section of a disk resonator. (a) A conformal oxide and electroplating mold are added to the a surface micromaching process. (b) Electrode is plated between the

$$\omega_o = \omega_{RF} - \omega_{LO}\,. \tag{21}$$

The resultant force acting on the resonator is given by

$$F = \frac{1}{2}[(V_P + v_{LO}) - v_i]^2 \frac{\partial C_{o1}}{\partial r} \tag{22}$$

where $\partial C_{o1}/\partial r$ can be expanded as the Taylor series [12]

$$\frac{\partial C_{o1}}{\partial r} = \frac{C_{o1}}{d}(1 + A_1 r + A_2 r^2 + A_3 r^3 \ldots)\,. \tag{23}$$

Substituting (19) and (23) into (22), results in a series of forces acting at varying frequencies; the most important of which acts at the resonant frequency with a magnitude given by

$$|F_{res}| = \frac{C_o V_{LO} V_{RF}}{2d}\,. \tag{24}$$

This in-band force is effectively multiplied by the Q of the resonator, resulting in vibration at the resonant frequency and output motional current separated from drive parasitics in the frequency domain. Because the inputs are at a much greater frequency than ω_o, they may easily be filtered, resulting in an output current due completely to motion of the resonator with no parasitic effects from C_o.

V. Fabrication

The need for submicron, high-aspect ratio, lateral electrode-to-resonator gaps in the disk resonator of Fig. 1 constitutes the most daunting requirement on the fabrication technology. Although 1000 Å lateral gaps have been achieved previously in µmechanical structures using e-beam lithography [13], this approach was found to be both time consuming and costly. In addition, if impedances on the order of 50Ω are desired, 1000 Å gaps may not be sufficient, and even smaller gaps on the order of 300 Å may in fact be desired [11]. To avoid the limitations of lithography and dry etching, the fabrication technology of this work combines surface micromachining, metal electroplating, and a sacrifi-

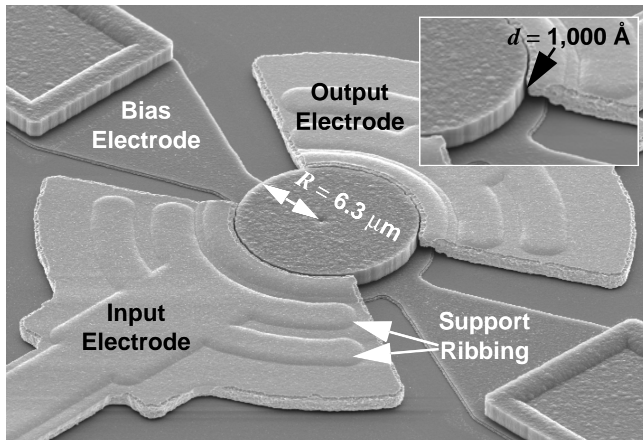

Fig. 9: SEM of a fabricated 433MHz (1st mode) disk resonator.

cial sidewall-spacer technique to achieve lateral polysilicon disk resonators with metal electrodes and submicron lateral electrode-to-resonator gaps, all without the need for aggressive lithographic or etching capability.

Figure 8 presents a pair of cross sections from the process flow. The initial process steps are identical to those used in previous polysilicon surface micromachining processes [9] to achieve a cross-section where a 2 μm-thick polysilicon layer, patterned to form the disk structure, is temporarily supported by a 5000 Å first sacrificial oxide layer. Instead of releasing the structure at this point, as would be done in a conventional surface micromachining process, this process continues with the conformal deposition of 1000 Å of LPCVD oxide to cover the sidewalls of the structure and serve as the gap-defining sacrificial layer. Next, the sacrificial oxide and the underlying oxide are etched to open anchors to the substrate passivation layers, and a metal seed layer is evaporated onto the wafer and removed from the top and sides of the structure in order to prevent plating in these areas. A thick photoresist mold is then deposited and patterned to define the electrodes, resulting in the cross-section of Fig. 8(a). This is followed by plating of the electrodes, using the PR as one portion of the mold and the sidewall of the structure as the other, plating directly against the sacrificial oxide layer. The PR and seed layer are then stripped, and the structure is released in HF to achieve the final cross-section shown in Fig. 8(b). The result: A disk suspended over the substrate by a single anchor in the middle, and separated from the plated electrodes by a thin air gap defined by the sacrificial layer. The minimum gap thickness in this process is limited only by the ability to control the thickness of a conformally deposited oxide film, and is independent of lithography and etching. A more thorough treatment of this process technology is given in [14]. Figure 9 presents a scanning electron micrograph (SEM) of a fabricated and released 433 MHz disk resonator, and the inset shows a close-up of this same resonator, offering a clearer view of its 1000 Å electrode-to-resonator gap. The support ribbing visible underneath the plated electrodes adds lateral support to the metal, helping to improve adhesion to the substrate.

VI. Experimental Results

The RF/LO measurement technique is the most robust method for characterizing experimental disk resonators and is therefore the method employed to evaluate the resonators of this work. A more thorough comparison of the techniques is carried out in [10]. All tests are carried out in a custom built vacuum chamber, capable of operating between 50 μTorr and atmospheric pressure. The basic resonator parameters are evaluated (*i.e.,* center frequency and quality factor), and the effects of pressure and temperature on performance are also assessed.

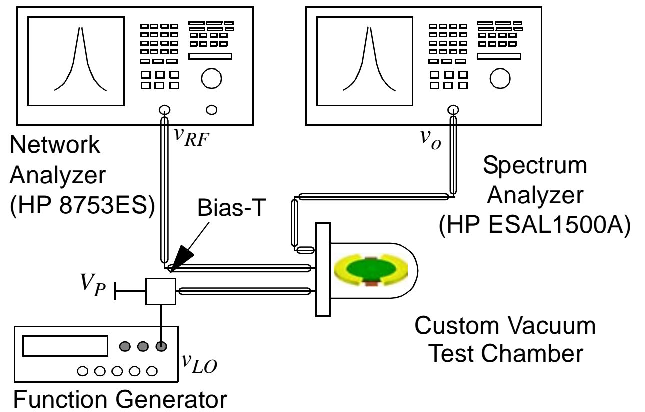

Fig. 10: Test setup for RF/LO measurement.

A. Resonator Performance

The test setup in Fig. 10 is used to implement the RF/LO measurement scheme described in Section IV. A network analyzer or other swept signal source provides the RF signal, while a function generator supplies the LO to the bias port via a bias-T. The output signal is measured on a spectrum analyzer. The disadvantage of this technique is that the spectrum analyzer is not well suited to swept measurements of this sort, requiring a maximum sample-and-hold technique or computer control to capture the necessary data. However, the RF/LO technique is more robust and extensible to higher frequencies than other measurement methods.

Figure 13 shows three spectra obtained via RF/LO measurements from a single 13.7μm radius disk resonator operating in the first three radial modes. In the fundamental mode, the resonator operates at 193 MHz with a Q in excess of 23,000. The second mode is at 515 MHz with a Q of approximately 9,000, and the third mode is centered at 829 MHz. Unfortunately, even using this measurement technique, other non-linearities in the measurement setup begin to dominate, yielding a peak height of just over 2 dB — insufficient to extract the Q. Note that the vertical axis for the RF/LO measurements is given in units of actual power measured at the output port (in dBm) rather than in relative power (dB), as the measurement data is collected on the spectrum analyzer rather than the network analyzer, and it represents the output power of the mixed product. A variety of resonators have been tested, and for the fundamental mode, the highest frequency measured was 433 MHz for a

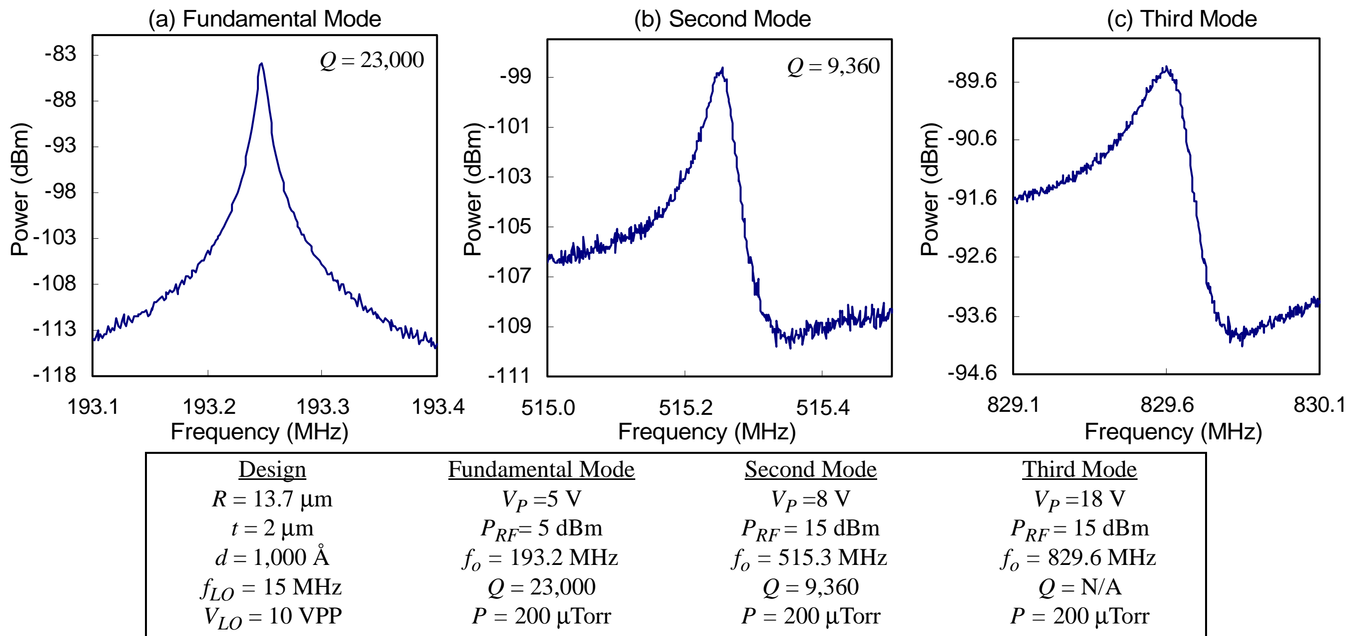

Fig. 13: A 13.7µm radius disk resonator tested in the (a) fundamental, (b) second, and (c) third modes via the RF/LO measurement technique.

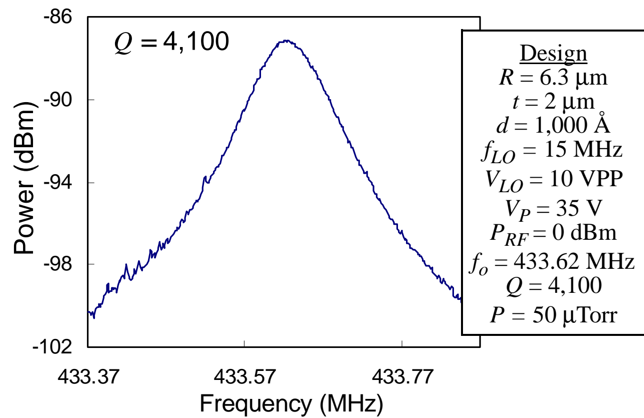

Fig. 11: Output spectra for a 433MHz (1st mode) disk resonator obtained via mixing.

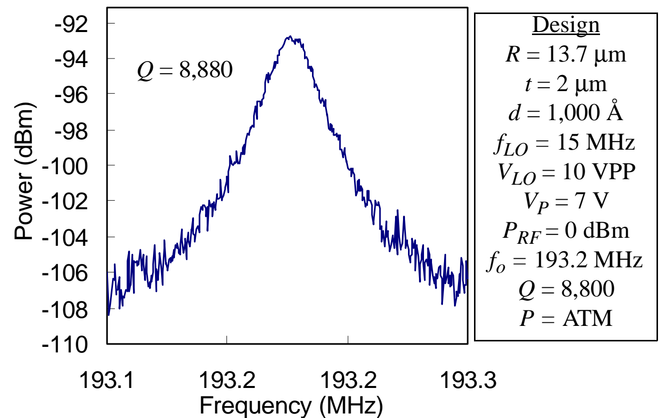

Fig. 12: The resonator of Fig. 13 measured at atmospheric pressure.

6.3 µm radius disk with a Q of over 4,000, shown in Fig. 11. Of the resonators measured, the results in Fig. 13 show the best response for the second mode, while the third mode has been measured with Q's as high as 3,200 at 317 MHz.

B. Effects of Pressure and Temperature

As indicated, all of the results in Fig. 11 and 13 were obtained with the resonator operating under vacuum levels of 200µTorr or less, and previous resonators [2,9,11] required vacuum in order to obtain acceptable quality factors. The spectrum in Fig. 12 was obtained from the same resonator measured in Fig. 13, but operated in the fundamental mode at atmospheric pressure. The Q remains high at 8,800, which is still better than most macroscopic resonators used in wireless applications at this frequency. Figure 14 shows a plot of the quality factor versus pressure for a similar disk resonator. Earlier resonators [16] typically required vacuum levels of 1mTorr or less in order to exhibit their maximum Q. For the disk resonator, this vacuum *threshold* has increased to roughly 10Torr and the Q remains above 10,000 even at pressures in excess of 100Torr.

Disk resonators are able to maintain high Q at atmospheric pressure due to their high stiffness in comparison to other types of resonators — rearranging (10),

$$Q = \frac{k_r}{c_r \omega_o} \tag{25}$$

At atmospheric pressure, damping is dominated by fluidic air damping, which acts at roughly the same magnitude in disk resonators as other types of resonator. However, the equivalent stiffness at a given frequency for disk resonators is much larger than previous types [2, 9, 16], greatly increasing the quality factor in air. Because these resonators can perform well in atmosphere, the need for vacuum packaging is eliminated for many applications, removing a significant barrier to the implementation of micromechanical resonators in practical wireless systems.

Another important resonator performance parameter is the *temperature coefficient of frequency*, or TC_f. In disk resona-

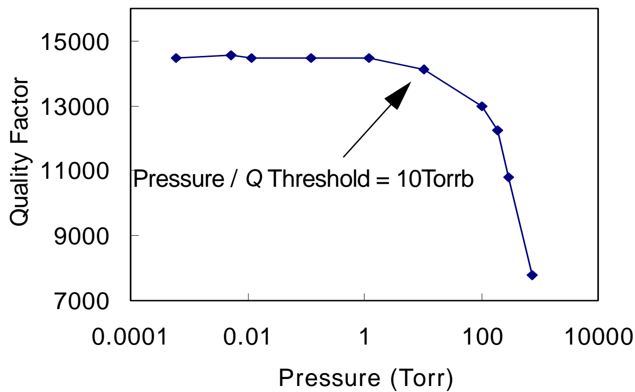

Fig. 14: Plot of quality factor versus pressure for a 193MHz disk resonator operating in the first mode.

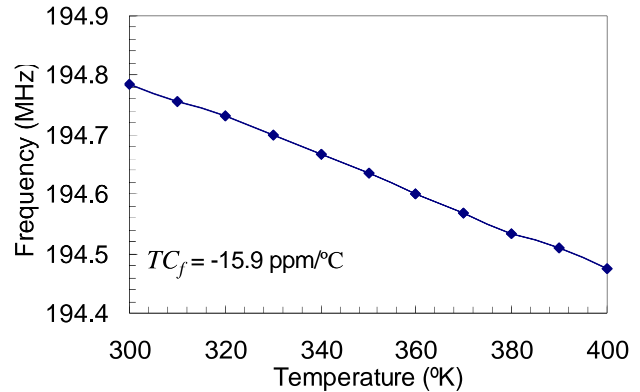

Fig. 15: Plot of resonant frequency versus temperature for a 193 MHz disk resonator similar to that measured in

tors, the variation in frequency with temperature is caused by the thermal expansion of the resonator material and the temperature dependence of Young's Modulus, which typically dominates the temperature response. Figure 14 shows a measured plot of frequency versus temperature for a 193 MHz disk resonator operated under conditions similar to those in Fig. 13(a). The extracted TC_f is about -16 ppm/ºC, which is similar to other micromechanical resonators [2], and the temperature curve is also linear, enabling simpler compensation methods than devices which show non-linear temperature characteristics.

VII. Conclusions

A laterally vibrating radial contour mode μmechanical disk resonator was presented with a measured frequency and *Q* as high as 433 MHz and 4,000, respectively, in the fundamental mode. In addition, resonators were demonstrated with *Q*'s as high as 23,000 in the fundamental mode at 193 MHz. Operation in the second overtone was demonstrated at 515 MHz with a *Q* of 9,300, and operation in the third overtone was demonstrated with *Q*'s up to 3,200 at 317 MHz and at frequencies up to 829 MHz. Disk resonators were also demonstrated operating at atmospheric pressure with *Q's* nearing 9,000, greatly reducing the need for and cost associated with vacuum packaging. These results push the operating frequencies of micromechanical resonators well into the UHF range and even into the U.S. cellular frequency band, where they sit poised to break the 1 GHz barrier. Such performance will enable revolutionary signal processor concepts (e.g., an RF channel selector at the front-end of a wireless receiver) [4] with substantial potential for lowering power consumption in wireless handsets.

References

[1] M. Roukes, "Nanoelectromechanical systems", *Proceedings of the Solid State Sensor and Actuator Workshop*, Hilton Head Island, South Carolina, June 4-8, 2000, pp. 367-376.

[2] K. Wang, Y. Yu, A.-C. Wong, and C. T.-C. Nguyen, "VHF free-free beam high-*Q* micromechanical resonators," *Proceedings*, 12th International IEEE MicroElectroMechanical Systems Conference, Orlando, Florida, Jan. 17-21, 1999, pp. 453-458.

[3] M. A. Abdelmoneum, M. U. Demirci, and C. T.-C. Nguyen, "Stemless wine-glass-mode disk micromechanical resonators," *Proceedings,* 16th International IEEE MicroElectroMechanical Systems Conf., Kyoto, Japan, Jan. 19.-23, 2003, pp. 698-701.

[4] C. T.-C. Nguyen, "Transceiver front-end architectures using vibrating micromechanical signal processors (invited)," *Dig. of Papers,* Topical Meeting on Silicon Monolithic Integrated Circuits in RF Systems, Sept. 12-14, 2001, pp. 23-32.

[5] C. T.-C. Nguyen, "Micromechanical components for miniaturized low-power communications (invited)," *Proceedings,* 1999 IEEE MTT-S International Microwave Symposium RF MEMS Workshop, Anaheim, California, June 18, 1999, pp. 48-77.

[6] J. R. Vig, Y. Kim, "Noise in microelectromechanical system resonators," *IEEE Transactions on Ultrasonics, Ferroelectrics, and Frequency Control,* vol. 46, no. 6, 1999, pp 1558-1565.

[7] M. Onoe, "Contour vibrations of isotropic circular plates," *Jour. of the Acoustical Soc. of America*, vol. 28, no. 6, 1956, pp 1158-1162.

[8] R. A. Johnson, *Mechanical Filters in Electronic*s, Wiley, 1983.

[9] F. D. Bannon, J.R. Clark, C.T.-C. Nguyen, "High-*Q* HF micromechanical filters," *IEEE JSSC*, vol. 35, no. 4, 2000, pp 512-526.

[10] J. R. Clark, W. T. Hsu, C. T-C. Nguyen, "Measurement techniques for capacitively-transduced VHF-to-UHF micromechanical resonators," *Proceedings,* Transducers '01, Munich, Germany, vol. 2, 2001, pp. 1118-1121.

[11] A.-C. Wong, H. Ding, C. T.-C. Nguyen, "Micromechanical mixer+filters," *Tech. Dig. of the 1998 IEED International Electron Devices Meeting*, San Francisco, CA, 1998, pp. 471-474.

[12] R. Navid, J.R. Clark, M. Demirci, C.T.-C. Nguyen, "Third-order intermodulation distortion in capacitively-driven CC-beam micromechanical resonators," *Proceedings,* 14th Int. IEEE MicroElectroMechanical Systems Conf., Interlaken, Switzerland, 2001, pp. 228-231.

[13] J.W. Weigold, A.C. Wong, C.T.-C. Nguyen, S.W. Pang, "Merged process for thick single-crystal Si resonators and BiCMOS circuitry," *JMEMS*, vol. 8, no. 3, 1999, pp. 221-228.

[14] W.T. Hsu, J.R. Clark, C.T.-C. Nguyen, "A sub-micron capacitive gap process for multiple-metal-electrode lateral micromechanical resonators," *Proceedings,* 14th Int. IEEE MicroElectroMechanical Systems Conf., Interlaken, Switzerland, 2001, pp. 349-352.

[15] K. Wang and C. T. C. Nguyen, "High-order medium frequency micromechanical electronic filters," *Journal of Microelectromechanical Systems*, vol. 8, no. 4, Dec., 1999, pp. 534-556.

[16] W. C. Tang, T.-C. H. Nguyen, and R. T. Howe, "Laterally driven polysilicon resonant microstructures," *Sensors and Actuators*, vol. 20, n. 1, Nov. 15, 1989, pp. 25-32.